

On steady and unsteady ship wave patterns

By D. E. NAKOS AND P. D. SCLAVOUNOS

Department of Ocean Engineering, Massachusetts Institute of Technology,
Cambridge MA 02139, USA

(Received 21 July 1989)

The properties of steady and unsteady ship waves propagating on a free surface discretized with panels are studied. The wave propagation is characterized by an explicit discrete dispersion relation which allows the systematic analysis of the distortion of the wave pattern due to discretization and the derivation of a stability criterion to be met by the numerical algorithm. The conclusions of the study are applied to a panel method used for the computation of steady and time-harmonic free-surface flows past elementary singularities and a ship hull.

1. Introduction

In recent years, numerous studies have attempted the solution of the invicid steady flow past ships by the distribution of Rankine singularities over the ship hull and part of the free surface, following the pioneering work of Dawson (1977) (see Aanesland 1986; P. S. Jensen, Mi & Söding 1986; G. Jensen 1988; P. S. Jensen 1987; Ni 1987; Raven 1988; Sclavounos & Nakos 1988; Van Beek, Piers & Sloof 1985; Xia & Larsson 1986). The principal motivation for adopting this approach is the enforcement of linearized free-surface conditions with variable coefficients, with the ultimate objective of the solution of the fully nonlinear problem. We lack, however, an adequate understanding of the nature of the distortion of the ship wave pattern caused by the discretization of the free surface. This is the subject of the present paper.

Linear gravity waves of frequency ω and vector wavenumber $\mathbf{k} = (u, v)$ propagating on the free surface obey a dispersion relation $\mathcal{W}(\omega, \mathbf{k}) = 0$, the form of which depends on the selection of the coordinate system relative to which the frequency ω is defined. Linearization and the homogeneity of the free-surface condition allow the Fourier decomposition of a wave disturbance as follows:

$$\iint d\mathbf{k} \frac{\tilde{f}(\mathbf{k})}{\mathcal{W}(\omega, \mathbf{k})} e^{i\mathbf{k}\cdot\mathbf{r}}, \quad (1.1)$$

where $\tilde{f}(\mathbf{k})$ is the Fourier transform of the forcing and \mathbf{r} is the horizontal radial vector from the origin of the coordinate system. The form of the wave-like component of this disturbance may be obtained from the large- \mathbf{r} asymptotics of the Fourier integral (1.1). Lighthill (1960) derived the relevant theory which relates the amplitude, wavelength and direction of propagation of waves found in direction \mathbf{r} to the dispersion relation *polar* in the (u, v) -plane and its gradients with respect to ω and \mathbf{k} . This theory is reviewed in §2 and is applied to the steady-state and time-harmonic surface waves propagating on a uniform stream.

This theory allows the characterization of waves propagating on a free surface which is discretized by plane quadrilaterals, as long as a dispersion relation

associated with the resulting discrete linear system can be defined. Assuming a polynomial variation of the velocity potential over each quadrilateral, the theory of discrete Fourier transforms may be applied as in Sclavounos & Nakos (1988) (hereinafter referred as A) to derive such a 'discrete' dispersion relation $\hat{W}(\omega, \mathbf{k}; F_h; \alpha) = 0$. This dispersion relation depends on two additional parameters arising from the discretization: the grid Froude number $F_h = U/(gh_x)^{1/2}$, where U is the forward speed and g the gravitational acceleration; and the ratio $\alpha = h_x/h_y$ of the panel dimensions in the streamwise and transverse directions. The consistency of the discretization requires that $\hat{W} \rightarrow \tilde{W}$ as $h_x, h_y \rightarrow 0$ with α kept finite constant. This condition is easy to satisfy in most numerical schemes. What determines if the waves propagate on the discretized free surface in a physically acceptable manner is the form of \hat{W} for finite F_h and α .

A free surface discretized by panels may therefore be regarded as a medium that admits the dispersion relation $\hat{W} = 0$. A rectangular free-surface panel mesh cannot resolve wavelengths smaller than $2h_x$ and $2h_y$ in the x - and y -directions, or wavenumbers (u, v) greater in modulus than the cut-off values $u^* = \pi/h_x$ and $v^* = \pi/h_y$, respectively. The effects of shorter waves are, however, indirectly present through *aliasing*. The discrete dispersion-relation polar has a periodic structure in both the u - and v -directions. Contributions to the wave disturbance from the points on the polar satisfying $|u| > u^*, |v| > v^*$ are reflected or aliased into the *principal wavenumber domain* $|u| \leq u^*, |v| \leq v^*$, carrying information from the short scales which cannot be directly resolved by the adopted panel dimensions. As h_x and h_y decrease, the principal wavenumber domain grows, the part of the discrete polar lying within it tends to its continuous limit and the periodic reflections of the discrete polar are removed to infinity.

Discretization errors may be quantified by comparing the location and gradients of the discrete and continuous dispersion-relation polars lying in the principal wavenumber domain. The largest errors occur to the components of the wave disturbance with wavenumbers near the cut-off values u^* and v^* . In §3, the theory of §2 is used to study the effects of discretization on the location, amplitude and direction of propagation of the numerical wave disturbance. In the steady problem, for example, an inappropriate selection of the parameters F_h and α for a consistent discretization, will lead to polars which allow waves to propagate at right angles to the incident stream, outside of the Kelvin wake. Consequently, consistency alone will not ensure a physically acceptable disturbance. It must be supplemented by a *stability* criterion which selects proper combinations of the parameters F_h and α in steady and time-harmonic problems.

The formal definition of stability of the numerical algorithm for steady and time-harmonic disturbances is given in §4. In the continuous problem, real wavenumbers \mathbf{k} always correspond to real ω , therefore defining a stable linear system. The discrete dispersion relation, on the other hand, may accept complex ω for real \mathbf{k} . In §4 a stability criterion is derived for both steady and time-harmonic flows which limits the freedom in the selection of the parameters F_h, α in a given numerical algorithm. Extensions of this stability analysis to transient free-surface flows are outlined in §5.

Section 6 illustrates the performance of a panel method based on a quadratic-spline approximation of the velocity potential used for the computation of steady and time-harmonic flows past a submerged wave source, a thin strut of infinite draught and the Wigley hull. Comparison with analytical solutions for the submerged source and the thin ship confirms the qualities of the numerical algorithm predicted by the theory of §§3 and 4.

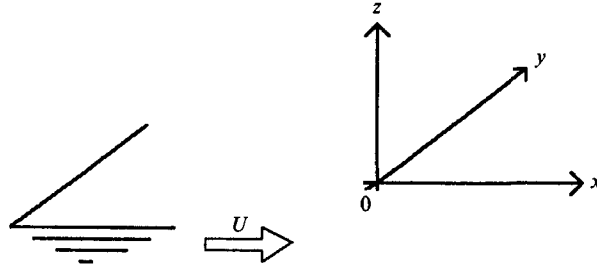


FIGURE 1. The Cartesian coordinate system.

2. The continuous dispersion relation

Consider a Cartesian coordinate system (figure 1) fixed relative to a disturbance which advances with constant velocity U in the negative x -direction. The origin is located on the mean position of the free surface and the z -axis points upwards. Assuming an inviscid and irrotational flow, the velocity potential ϕ governing the resulting linearized free-surface problem satisfies the Laplace equation in the fluid domain and is subject to the free-surface condition

$$\left(\frac{\partial}{\partial t} + U\frac{\partial}{\partial x}\right)^2 \phi + g\frac{\partial\phi}{\partial z} = 0, \quad z = 0, \tag{2.1}$$

where g is the gravitational acceleration.

In response to a time-harmonic excitation at a frequency ω , solutions subject to (2.1) accept the general Fourier decomposition on the mean position of the free surface

$$\phi(x, y) = \lim_{\epsilon \rightarrow 0^+} \left\{ \frac{1}{(2\pi)^2} \int_{-\infty}^{+\infty} du \int_{-\infty}^{+\infty} dv \frac{\tilde{f}(u, v)}{\mathcal{W}(u, v; \omega - i\epsilon)} e^{-1(ux+vy)} \right\}, \tag{2.2}$$

where

$$\mathcal{W}(u, v; \omega) = -(\omega - Uu)^2 + g(u^2 + v^2)^{\frac{1}{2}}. \tag{2.3}$$

The real part of all complex quantities is understood hereafter, with the complex factor $e^{i\omega t}$ omitted throughout. In (2.2) the Rayleigh viscosity $\epsilon > 0$ is introduced for the enforcement of the radiation condition. The forcing function $f(x, y)$ is assumed to possess a Fourier transform $\tilde{f}(u, v)$ which decays sufficiently rapidly as $|u|, |v| \rightarrow \infty$ for the integral (2.2) to be convergent. The solution (2.2) consists of a ‘local’ non-radiating disturbance and a ‘free-wave’ field. This decomposition can be formally justified by complex contour integration in (2.2).

Here attention will be focused on the free-wave field. The wavenumber vector $\mathbf{k} = (u, v)$ identifies a free-wave component forced at the frequency ω so long as it points to a curve in the (u, v) -plane defined by the dispersion relation

$$\tilde{\mathcal{W}}(u, v; \omega) = -\frac{\omega^2}{g} + \frac{2\omega U}{g}u - \frac{U^2}{g}u^2 + (u^2 + v^2)^{\frac{1}{2}} = 0. \tag{2.4}$$

This curve is hereafter referred to as the *dispersion-relation polar*. Given ω , the polar (2.4) consists of three or two branches depending on whether the parameter $\tau = \omega U/g$ is less or greater than the critical value $\tau_c = \frac{1}{4}$, respectively. Figure 2 illustrates the branches obtained for $\tau = 0, 0.2, 0.5, 1$. Each branch of (2.4) corresponds to a ‘wave system’. At the critical value $\tau_c = \frac{1}{4}$, the closed loop around the origin meets the branch which lies in the negative u -plane for $\tau < \frac{1}{4}$, and the corresponding wave

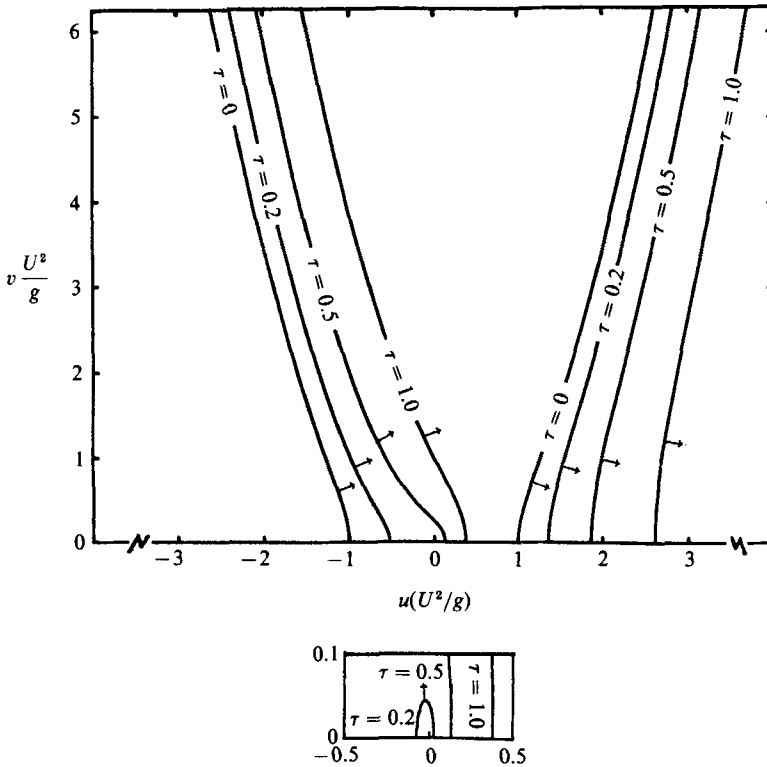


FIGURE 2. The polars of the continuous dispersion relation corresponding to $\tau = 0, 0.2, 0.5, 1.0$. The small figure at the bottom amplifies the region around the origin. The vectors drawn on the various branches of the polars show the direction of propagation of the corresponding wave systems.

systems merge for values of $\tau > \frac{1}{4}$. In the steady limit ($\omega = 0, U > 0$), the closed branch around the origin shrinks to zero, while the two open branches become symmetric with respect to the v -axis and end up representing a common wave system, the Kelvin wave pattern. All branches drawn in figure 2 are symmetric with respect to the u -axis owing to the symmetry of the flow about the $y = 0$ plane.

By applying the method of stationary phase to the Fourier integral (2.2) for large values of $r = (x, y)$, Lighthill (1960) derived an expression relating the free waves governed by the dispersion relation (2.4) to the shape of the dispersion relation polar and its gradients with respect to the (u, v) wavenumbers. The principal results of this analysis are summarized below.

A free-wave component corresponding to some point on the polar (2.4) is found in the direction pointed by the group-velocity vector

$$\mathbf{V}_g = -\frac{\nabla \tilde{W}(u, v; \omega)}{\partial \tilde{W}(u, v; \omega) / \partial \omega}, \tag{2.5}$$

which by definition is normal to the polar at the selected point. The choice between the two possible directions of this normal follows from the enforcement of the radiation condition which requires that the energy of each wave component must propagate towards infinity. Normal vectors pointing in the direction of the group velocity are drawn in figure 2 on the various branches of the dispersion-relation polar. For $\tau = 0.2$ the wave system associated with the closed branch covers the

entire free surface, while each of the two open branches defines wave systems that are included within sectors trailing the disturbance. Their half-angle is equal to the angle formed between the u -axis and the normal vector at the inflection point of the corresponding branch of the polar.

The velocity potential in the far field is, to leading order for large $r = |\mathbf{r}|$, proportional to

$$\phi(r, \theta) \sim \frac{\exp(i\mathbf{k} \cdot \mathbf{r})}{r^{\frac{1}{2}}} \frac{\tilde{f}}{|\kappa|^{\frac{1}{2}} |\nabla \mathcal{W}|}, \quad (2.6)$$

where θ is the angular position in the far field determined by the group-velocity vector (2.5) and κ is the curvature of the dispersion relation polar at the corresponding point. Expression (2.6) becomes singular when $\kappa = 0$, which occurs at inflection points of the polar. They correspond to the caustics of the wave disturbance and the asymptotic analysis that produced (2.6) must be revised to account for the coalescence of two stationary points leading to an $r^{-\frac{1}{2}}$ decay of the wave disturbance along the caustic. A second singular case arises when $|\nabla \mathcal{W}| = 0$ which, by virtue of (2.5), corresponds to the vanishing of the group velocity for some wave component. This is the case at $\tau = \frac{1}{4}$ and signifies the failure of linear theory to model the wave disturbance.

An important component of expression (2.6) is the magnitude of the Fourier transform of the forcing $\tilde{f}(u, v)$. It can be shown that if the 'wavemaking source' is a translating and/or oscillating fully submerged body, the corresponding \tilde{f} decays exponentially for large \mathbf{k} and the resulting free waves contain very little energy in the short scales. For a surface-piercing body on the other hand, \tilde{f} decays only algebraically and the corresponding wave field contains short waves carrying a significant amount of energy. The short waves are associated with the open branches of the dispersion relation which for large- \mathbf{k} have a slope such that the shortest waves are visible near the track of the disturbance, with their wavelength tending to zero along the track.

3. The discrete dispersion relation

A class of numerical methods solve the potential flow around realistic ship forms by the distribution of panels on the ship hull and part of the free surface. They can treat free-surface conditions with variable coefficients which are more accurate than (2.1) near the ship hull, which have also been used lately for the solution of the fully nonlinear problem (see G. Jensen 1988; Ni 1987).

In the linearized case, the principal scepticism about this approach, as opposed to methods that distribute wave singularities over the ship surface alone, relates to its ability to properly model the propagation of the wave disturbance on a discretized free surface. In this section, a dispersion relation is derived governing this wave propagation problem, hereafter referred to as the *discrete dispersion relation*, and the continuous and discrete wave patterns are compared by applying the theory of §2.

Consider the enforcement of the linearized free-surface condition (2.1) by a distribution of Rankine singularities over the free surface. Applying Green's second identity to the velocity potential $\phi(\mathbf{x})$ and the Rankine source potential $G(\mathbf{x}; \xi) = 1/2\pi r = 1/(2\pi|\mathbf{x} - \xi|)$, we obtain for any fixed \mathbf{x} on the $z = 0$ plane

$$\phi(\mathbf{x}) + \iint_{\text{FS}} \left(-\frac{\omega^2}{g} + 2i \frac{\omega U}{g} \frac{\partial}{\partial \xi} + \frac{U^2}{g} \frac{\partial^2}{\partial \xi^2} \right) \phi(\xi) G(\mathbf{x}; \xi) d\xi = \mathcal{R}(\mathbf{x}) = \iint_{\text{FS}} f(\xi) G(\mathbf{x}; \xi) d\xi, \quad (3.1)$$

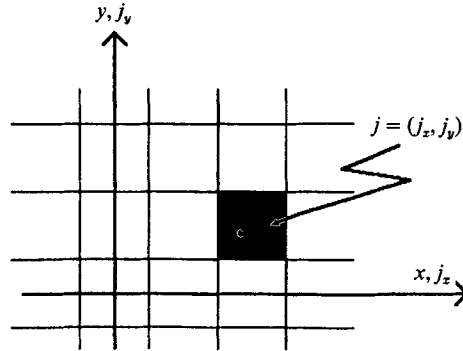


FIGURE 3. A portion of the free-surface mesh. The panels are numbered by the vector index $\mathbf{j} = (j_x, j_y)$, where j_x and j_y count in the x - and y -directions respectively.

where both integrations are carried out over the entire free surface (FS) and the forcing function $f(\mathbf{x})$ corresponds to a model applied pressure distribution, decaying fast enough at large distance from the origin so that the integral of the right-hand side of (3.1) is convergent for any finite \mathbf{x} . Moreover, at a fixed finite \mathbf{x} , the contribution from the closing surface at infinity vanishes owing to the $r^{-\frac{1}{2}}$ decay of ϕ and the r^{-1} decay of G as $|\xi| \rightarrow \infty$. The radiation condition will be enforced at a later stage of the solution procedure.

Taking the Fourier transform of the integral equation (3.1) with respect to the (x, y) -coordinates and applying the convolution theorem, the continuous solution is obtained in the explicit form (2.2), where $\tilde{\mathcal{W}}(u, v; \omega)$ is the ratio of the Fourier transforms of the integral operators of the left- and right-hand sides of (3.1), and it can be shown that it is given by (2.3).

The discretization of (3.1) starts with the definition of a rectangular grid on the free surface. For the derivation of the discrete dispersion relation it is appropriate to assume that the grid is of infinite extent and of uniform spacing h_x and h_y in the x - and y -directions respectively. The effect of a truncated free-surface grid on the wave propagation, and in particular with regard to the enforcement of the radiation condition, is discussed in §6. On this mesh, illustrated in figure 3, the unknown velocity potential is approximated by a linear combination of polynomial basis functions of finite support centred at the panel centroids, or

$$\phi(\mathbf{x}) \approx \phi_h(\mathbf{x}) = \sum_{\mathbf{j}} a_{\mathbf{j}} B_{\mathbf{j}}(\mathbf{x}). \quad (3.2)$$

The summation in (3.2) is carried out over the vector index $\mathbf{j} = (j_x, j_y)$, for all integer values of j_x and j_y . This compact summation notation is implied in the subsequent analysis, unless otherwise noted. The function $B_{\mathbf{j}}(\mathbf{x})$ is the basis function centred at the \mathbf{j} th panel and the constant $a_{\mathbf{j}}$ is the associated weight.

An essential characteristic of the numerical scheme is the method of treatment of the convective derivatives in (3.1). They may be evaluated analytically by direct differentiation of the underlying basis function $B_{\mathbf{j}}(\mathbf{x})$, or they may be approximated by finite-difference schemes. A number of alternative choices are derived and discussed in A for the steady problem. Here, we study a quadratic spline scheme using the quadratic B -spline as the basis function. The discrete solution (3.2) has continuous value and slope in both the x - and y -directions, which permits the analytical evaluation of the derivatives $(\partial/\partial\xi)$ and $(\partial^2/\partial\xi^2)$ in (3.1).

Substitution of (3.2) in (3.1) and collocation at the panel centroids x_j , leads to the discrete formulation:

$$\sum_j a_j \left\{ B_{ij} + \left(-\frac{\omega^2}{g} S_{ij}^{(0)} + 2i \frac{\omega U}{g} S_{ij}^{(1)} + \frac{U^2}{g} S_{ij}^{(2)} \right) \right\} = R_i, \tag{3.3}$$

where
$$B_{ij} = B_j(x_i) = B_{i-j}, \tag{3.4a}$$

$$S_{ij}^{(m)} = \iint_{-\infty}^{+\infty} \frac{\partial^m B_j(\xi)}{\partial \xi^m} G(x_i; \xi) d\xi = S_{i-j}^{(m)}, \quad m = 0, 1, 2, \tag{3.4b}$$

$$R_i = \mathcal{R}(x_i) = \iint_{-\infty}^{+\infty} f(\xi) G(x_i; \xi) d\xi. \tag{3.4c}$$

In analogy to the continuous problem, the theory of discrete Fourier transforms is applied to transform (3.3) in the Fourier space. It follows that

$$\hat{L}\hat{\phi}_h = \hat{R}, \tag{3.5}$$

with

$$\hat{L}(\hat{u}, \hat{v}; \omega; F_h, \alpha) = -\Omega^2 \Sigma_0(\hat{u}, \hat{v}; \alpha) + 2\Omega F_h \Sigma_1(\hat{u}, \hat{v}; \alpha) - F_h^2 \Sigma_2(\hat{u}, \hat{v}; \alpha) + 1, \tag{3.6}$$

where $\Omega = \omega(h_x/g)^{1/2}$ and the grid Froude number and panel aspect ratio are defined by

$$F_h = \frac{U}{(gh_x)^{1/2}}; \quad \alpha = \frac{h_x}{h_y}. \tag{3.7}$$

The quantities $\Sigma_m, m = 0, 1, 2$ are explicit functions of the non-dimensional wavenumbers $\hat{u} = uh_x/2\pi, \hat{v} = vh_y/2\pi$ and the panel aspect ratio α , and are defined by

$$\Sigma_m(\hat{u}, \hat{v}; \alpha) = (2\pi)^{m-1} \frac{\sum_{k, l=-\infty}^{+\infty} \frac{(-)^{k+l}}{(k+\hat{u})^{3-m}(l+\hat{v})^3 [(k+\hat{u})^2 + \alpha^2(l+\hat{v})^2]^{3/2}}}{\sum_{k, l=-\infty}^{+\infty} \frac{(-)^{k+l}}{(k+\hat{u})^3(l+\hat{v})^3}}, \quad m = 0, 1, 2. \tag{3.8}$$

From this definition it follows that the functions $\Sigma_m, m = 0, 1, 2$ are periodic in both u and v , with periods $2\pi/h_x$ and $2\pi/h_y$ respectively. The consistency of the numerical algorithm may be established by studying the small h_x, h_y limit of Σ_m . It follows from the Taylor expansion of (3.8) for small \hat{u} and \hat{v} that

$$\lim_{\hat{u}, \hat{v} \rightarrow 0} \Sigma_m(\hat{u}, \hat{v}; \alpha) = (2\pi)^{m-1} \frac{\hat{u}^m}{(\hat{u}^2 + \alpha^2 \hat{v}^2)^{3/2}} = (h_x)^{m-1} \frac{u^m}{(u^2 + v^2)^{3/2}}, \quad m = 0, 1, 2. \tag{3.9}$$

The details of the derivation of expression (3.8) and its limit (3.9) can be found in A.

Equation (3.5) can be transformed back to the real space by using the inverse discrete Fourier transform, leading to the following expression for ϕ_h :

$$\phi_h(x_j, y_j) = \frac{1}{(2\pi)^2} \int_{-\pi/h_x}^{\pi/h_x} du \int_{-\pi/h_y}^{\pi/h_y} dv \frac{\hat{R}}{\hat{L}} e^{-i(ux_j + vy_j)}, \tag{3.10}$$

valid only pointwise at the collocation points (x_j, y_j) . The variation of the discrete solution at intermediate points over the free surface is determined by (3.2). The finite limits of integration in (3.10) signify that variation due to wave components of wavelength smaller than the cut-off wavelengths $2h_x$ and $2h_y$ cannot be resolved on the (h_x, h_y) -grid. The two-dimensional range of integration in (3.11), $|u| \leq \pi/h_x, |v| \leq \pi/h_y$, is hereafter referred to as the principal wavenumber domain.

The energy of shorter waves is, however, reflected into the principal wavenumber domain through the phenomenon of *aliasing*. Using the Poisson summation formula, the discrete Fourier transform of the forcing function, \hat{R} , may be expressed in the form

$$\hat{R}(u, v; h_x, h_y) = \sum_{k, l=-\infty}^{\infty} \tilde{\mathcal{H}}\left(u + \frac{2\pi k}{h_x}, v + \frac{2\pi l}{h_y}\right) = \sum_{k, l=-\infty}^{\infty} \frac{\tilde{f}\left(u + \frac{2\pi k}{h_x}, v + \frac{2\pi l}{h_y}\right)}{\left[\left(u + \frac{2\pi k}{h_x}\right)^2 + \left(v + \frac{2\pi l}{h_y}\right)^2\right]^{\frac{1}{2}}}, \quad (3.11)$$

where the effect of aliasing becomes transparent. Substituting (3.11) into (3.10) and taking advantage of the periodicity of \hat{L} , the limits of integration in (3.10) can be extended to $\pm\infty$ leading to the following alternative expression for the discrete solution:

$$\phi_h(x_j, y_j) = \frac{1}{(2\pi)^2} \int_{-\infty}^{+\infty} du \int_{-\infty}^{+\infty} dv \frac{\tilde{f}(u, v)}{\hat{W}(u, v; \omega; F_h, \alpha)} e^{-i(ux_j + vy_j)}, \quad (3.12)$$

with
$$\hat{W}(u, v; \omega; F_h, \alpha) = (u^2 + v^2)^{\frac{1}{2}} \hat{L}(u, v; \omega; F_h, \alpha). \quad (3.13)$$

In view of (3.12), it follows that the discrete dispersion relation is defined as

$$\hat{W}(u, v; \omega; F_h, \alpha) = 0. \quad (3.14)$$

The theory of §2 is next applied for the description of the time-harmonic wave disturbance excited at the frequency ω . The comparison of the continuous and discrete dispersion relations (2.4) and (3.14) reveals the differences between the respective wave fields and is used to establish the stability and convergence of the adopted numerical scheme.

Polars of (3.14) are illustrated in figure 4(a) for $\tau = \omega U/g = 0, 0.2, 0.5, 1$ and ($F_h = \sqrt{2}, \alpha = 1$). All polars are symmetric about the u -axis and periodic in the u - and v -directions, with periods $2\pi/h_x$ and $2\pi/h_y$ respectively. It is, therefore, sufficient to display only the upper half of the principal wavenumber domain. As in the continuous problem, pairs of (u, v) that solve (3.14) lie either on three or two separate branches, depending on whether τ is less or greater than the critical value τ_c , which owing to discretization is slightly shifted from the value $\frac{1}{4}$ of the continuous problem. The same figure shows the corresponding polars of the continuous dispersion relation which are found to be in very good agreement with the discrete polars only over the inner portion of the principal wavenumber domain.

The polars of the discrete dispersion relation, for the same frequencies but a different panel mesh ($F_h = 1, \alpha = 4$), are shown in figure 4(b). The topology of this set of discrete polars is seen to be drastically different from that of their continuous counterparts, in particular close to the boundaries of the principal wavenumber domain. Crossing of polars corresponding to different frequencies signifies the inversion of the direction of propagation of the associated wave components, rendering them physically unacceptable. It will be shown in §4, that the grid ($F_h = 1, \alpha = 4$) corresponds to an unstable scheme.

A convergent numerical algorithm must be consistent and stable. Consistency is here ensured by verifying that for all finite u and v the discrete and continuous dispersion relation polars coalesce in the limit as $h_x, h_y \rightarrow 0$. This condition is easy to show by substituting in (3.6)–(3.13) the limiting values of $\Sigma_m, m = 0, 1, 2$ given by (3.9). A byproduct of consistency is the order of the method, defined as the rate at which the continuous and discrete polars approach each other. It is shown in A that the present quadratic-spline scheme is of $O(h_x^3)$.

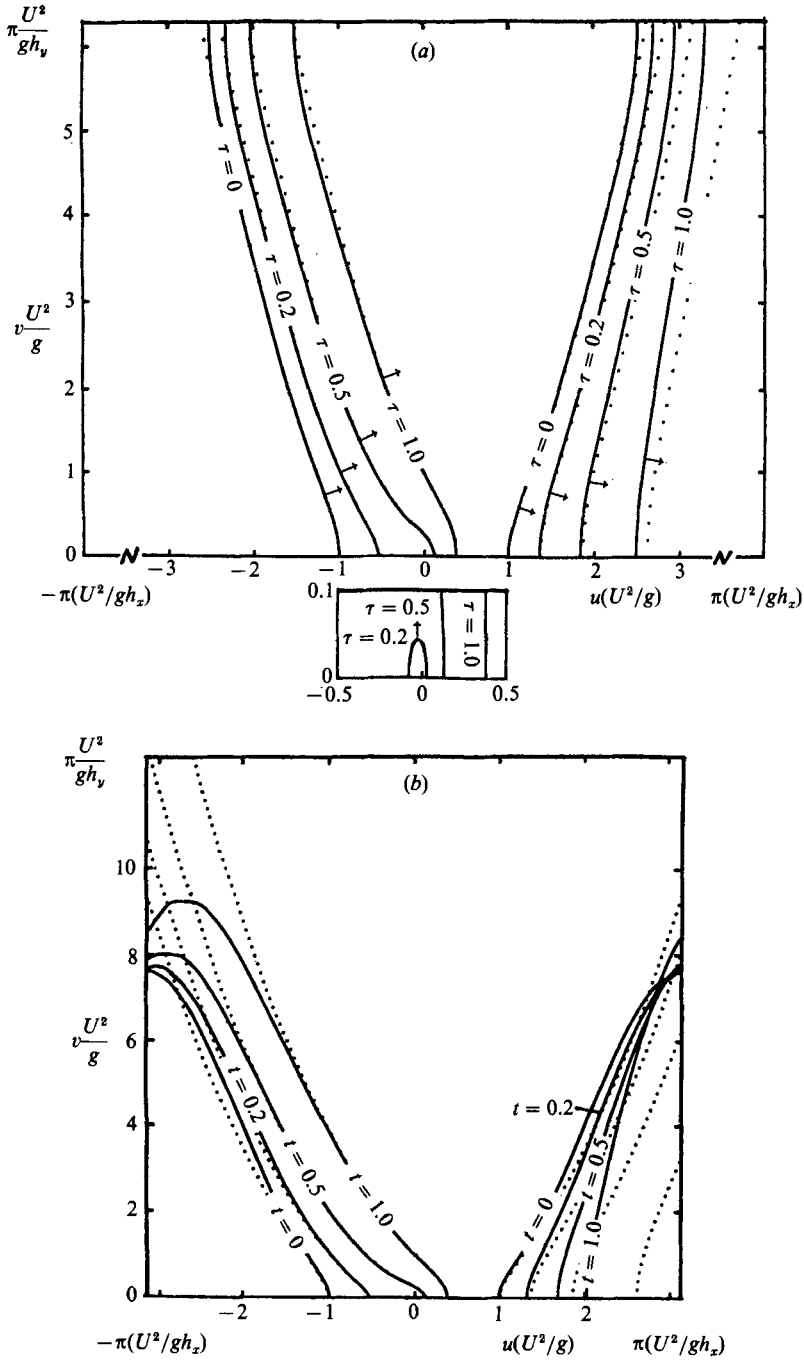


FIGURE 4. The polars of the discrete dispersion relation corresponding to $\tau = 0, 0.2, 0.5, 1.0$ and the grids (a) ($F_h = \sqrt{2}, \alpha = 1$), and (b) $F_h = 1, \alpha = 4$), over the principal wavenumber domain. The dotted lines show the corresponding polars of the continuous dispersion relation. The small figure amplifies the region around the origin. The vectors drawn on the various branches of the polars show the direction of propagation of the corresponding wave systems.

As h_x, h_y decrease, the size of the principal wavenumber domain increases and the disparity between the continuous and discrete polars is removed to infinity. In actual computations, however, the panel dimensions are kept finite, and the short scales corresponding to wavenumbers u and v comparable to or larger than the cut-off values π/h_x and π/h_y respectively are substantially distorted relative to their continuous limit.

A closer examination of this discretization error is illustrated in figure 5(a), where the polars of the discrete dispersion relation for $\tau = 0$ are compared to their continuous counterparts over a larger portion of the wavenumber space. The grid parameters are taken to be $F_h = 1$ and $\alpha = 1$. As discussed earlier, the discrete polars are in very close agreement with the continuous ones close to the origin, departing from them at larger wavenumbers, especially outside the principal wavenumber domain. Using the theory presented in §2, the direction of propagation of the various wave components that satisfy the discrete dispersion relation, as well as the associated wave amplitude in the far-field, can be deduced from the geometrical characteristics of the polars shown in figure 5(a).

The direction in the far field where a wave component corresponding to the point A on the discrete polar will be observed, is defined by the vector normal to the polar at the point A , shown in figure 5(a). As the point A moves on the polar from $v = 0$ to $v = \pi/h_y$, the group-velocity vector forms an angle with the x -axis which increases from zero at $v = 0$ to its maximum value at the inflection point K and then decreases to zero at $v = \pi/h_y$, owing to the v -periodicity of the polar. The inflection point corresponds to the wave component along the Kelvin angle, which in the discrete problem differs slightly from 19.5° , owing to discretization error. The corresponding variation on the continuous polar shown in the same figure is quite similar for small and moderate wavenumbers inside the principal wavenumber domain, while larger discrepancies occur at wavenumbers v comparable to or greater than π/h_y . In particular, the shortest wave component that can be resolved by the adopted grid is found along the track of the disturbance in the discrete solution, although according to the continuous dispersion relation it should be visible at a small angle off the track.

The difference between the continuous and discrete polars is more dramatic in figure 5(b) which corresponds to the same $F_h = 1$, but a different panel aspect ratio, $\alpha = 4$. Here the discrete polar permits steady-state wave components to be visible at right angles to the track of the disturbance, therefore defining a numerical Kelvin angle of 90° . Such physically unacceptable wave fields are also possible in the unsteady case and correspond to the discrete polar topologies shown in figure 4(b). It will be shown in §4 that this topology corresponds to unstable schemes.

Owing to the periodicity of the polars, there exists an infinity of points A_{ki} with a normal of the same direction to that at point A . This doubly infinite array of points represents a collection of wave disturbances of disparate wavelengths occurring in the same angular direction in the far field. Of all these wave components, only the one corresponding to the point $A_{00} \equiv A \equiv (u_A, v_A)$ in the principal wavenumber domain can be resolved by the adopted discretization. Its amplitude is, however, affected by the cumulative contribution of all the other shorter wave components which, by virtue of (3.12), are weighted by the decaying amplitude of the spectrum $\hat{f}(u, v)$ at the corresponding reflection of A . This 'reflection' of the energy of wave components which cannot be resolved by the free-surface grid into the principal wavenumber domain is called *aliasing*.

The discretization error is quantified by the application of (2.5) and (2.6) to (3.12).

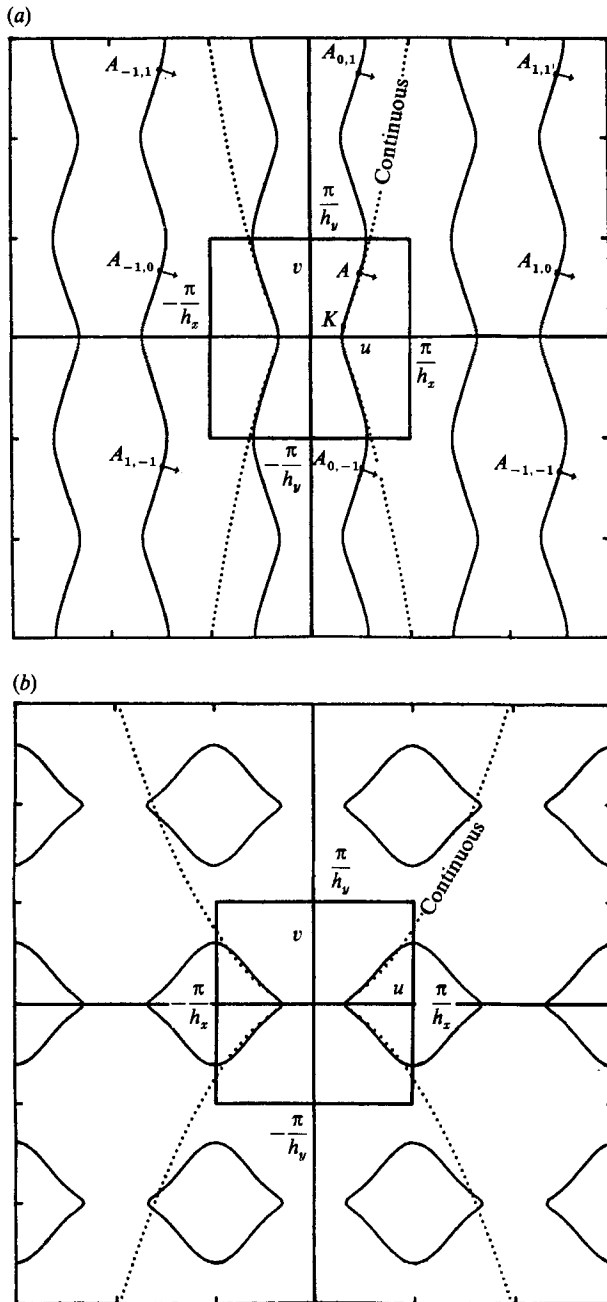


FIGURE 5. The periodic structure of the polars of the discrete dispersion relation at $\tau = 0$ and for the grids (a) ($F_h = 1, \alpha = 1$), and (b) ($F_h = 1, \alpha = 4$). The squared region in the middle is the principal wavenumber domain. The dotted lines show the corresponding polars of the continuous dispersion relation. All of the marked points A_{ki} show the wave components whose energy gets aliased on the one principal wave component denoted by A .

The velocity potential of the numerical wave disturbance in the far field, to leading order for large $r_j = |\mathbf{r}_j| = |(x_j, y_j)|$, is proportional to

$$\begin{aligned} \phi_h(r_j, \theta) &\sim \frac{1}{(2\pi r_j)^{\frac{1}{2}}} \sum_{k, l=-\infty}^{\infty} \frac{\tilde{f}(A_{kl})}{|\kappa(A_{kl})|^{\frac{1}{2}} |\nabla \hat{W}(A_{kl})|} \exp(i\mathbf{k}_{A_{kl}} \cdot \mathbf{r}_j) \\ &= \frac{1}{(2\pi r_j)^{\frac{1}{2}}} \frac{1}{|\kappa(A)|^{\frac{1}{2}}} \frac{1}{|\nabla \hat{L}(A)|} \exp(i\mathbf{k}_A \cdot \mathbf{r}_j) \sum_{k, l=-\infty}^{\infty} \frac{\tilde{f}\left(u_A + \frac{2\pi k}{h_x}, v_A + \frac{2\pi l}{h_y}\right)}{\left[\left(u_A + \frac{2\pi k}{h_x}\right)^2 + \left(v_A + \frac{2\pi l}{h_y}\right)^2\right]^{\frac{1}{2}}}, \end{aligned} \quad (3.15)$$

where θ is the angular position in the far field defined by the group-velocity vector (2.5) corresponding to the point A , and $\kappa(A)$ is the common curvature of the discrete polar at the points A_{kl} .

The wavelength found at the angular position θ in the far field of the numerical solution differs from that of the continuous solution owing to the disparate locations of the continuous and discrete polars. This discrepancy in the wavelengths is referred to as 'numerical dispersion'. The corresponding amplitude of the numerical solution is affected by the discretization error not only via the different gradient and curvature of (2.4) and (3.14), but also owing to aliasing. Evidently, the effect of aliasing is more pronounced for excitations of the slowly decaying spectrum of the forcing, $\tilde{f}(u, v)$, as $|u|, |v| \rightarrow \infty$.

4. Stability of the discretization scheme

A discrete dispersion relation may be defined for any selection of the parameters of the numerical algorithm, but only a subset of stable selections of its parameters results in a 'physically acceptable' wave disturbance. This section derives such a stability criterion which restricts the choice of the panel aspect ratio α , the grid Froude number $F_h = U/(gh_x)^{\frac{1}{2}}$ and the reduced frequency $\tau = \omega U/g$.

The stability analysis of numerical schemes for the solution of partial differential equations of mathematical physics typically applies to initial-value problems and requires that the numerical solution remains bounded in time, under the assumption of harmonic variation in space. The present analysis studies the stability of the flow under the assumption that it has reached a steady-state time-harmonic limit. The stability condition is therefore not related to boundedness in time, assumed by the harmonic time dependence, but is associated to the well-posedness of this steady-state limit.

In the continuous problem, any selection of the wavenumber vector $\mathbf{k} = (u, v)$ corresponds to two distinct real frequencies ω . This follows from the continuous dispersion relation (2.3) and (2.4), regarded as a quadratic equation for ω . The discrete dispersion relation (3.14) on the other hand, accepts real roots for the frequency ω only for values of \mathbf{k} that render the discriminant

$$\Delta(\hat{u}, \hat{v}; F_h, \alpha) = F_h^2[\Sigma_1^2(\hat{u}, \hat{v}; \alpha) - \Sigma_0(\hat{u}, \hat{v}; \alpha) \Sigma_2(\hat{u}, \hat{v}; \alpha)] + \Sigma_0(\hat{u}, \hat{v}; \alpha) \quad (4.1)$$

positive. The vanishing of Δ for a wave component $\mathbf{k} = (u, v)$ which also satisfies the discrete dispersion relation

$$\hat{W}(u, v; \omega) = 0, \quad (4.2)$$

is equivalent to the equation

$$\frac{\partial \hat{W}(u, v; \omega)}{\partial \omega} = 0, \quad (4.3)$$

which, by virtue of (2.5), corresponds to an infinite group velocity for the wave components satisfying (4.2) and (4.3). This condition will next be shown to be equivalent to the existence of a non-unique solution for the time-harmonic wave disturbance governed by the dispersion relation $\hat{W} = 0$ signifying the onset of instability in the discrete problem.

The continuous and discrete solutions represented by (2.2) and (3.12) respectively represent non-unique wave disturbances, unless a radiation condition is satisfied. For a time-harmonic wave disturbance of frequency ω it can be enforced by shifting the real frequency ω to the complex value $\omega - i\epsilon$, where the Rayleigh viscosity ϵ is a small positive constant. The effect of this complex shift of the frequency is to displace the poles of (2.2) and (3.12) in the complex u - and v -planes by amounts proportional to $i\epsilon \partial \tilde{W} / \partial \omega$ and $i\epsilon \partial \hat{W} / \partial \omega$ respectively. It is evident from (2.3) and (2.4) that $\partial \tilde{W} / \partial \omega \neq 0$ for all (u, v) subject to the continuous dispersion relation. In the case of the discrete dispersion relation, however, and when $\partial \hat{W} / \partial \omega = 0$, the corresponding pole is *pinched* on real values of (u, v) , in spite of the Rayleigh shift of the frequency. Since the radiation condition for the associated wave component cannot be enforced, the problem is ill-conditioned, accepting multiple solutions, and the numerical scheme becomes unstable.

Unstable wavenumbers $\mathbf{k} = (u, v)$, should they exist, are solutions of the system of transcendental equations (4.2) and (4.3), where the latter may be replaced by the equivalent condition

$$\Delta(u, v; F_h, \alpha) = 0, \quad (4.4)$$

which is independent of the frequency. A condition between the parameters ω, F_h and α is sought such that there exist pairs (u, v) that satisfy both (4.2) and (4.4). Owing to the periodicity and symmetry properties of \hat{W} and Δ in the u - and v -directions, it is sufficient to seek the intersection of the curves (4.2) and (4.4) in the upper half of the principal wavenumber domain, $|u| \leq \pi/h_x, 0 \leq v \leq \pi/h_y$.

Figure 6 plots the curve (4.4) for the grid ($F_h = 1, \alpha = 1$), which divides the principal wavenumber domain into the shaded regions symmetric about the v -axis, which correspond to $\Delta < 0$, and the unshaded region which corresponds to $\Delta > 0$. The discrete dispersion-relation polars for these values of F_h and α lie in the unshaded region since they all correspond to real frequencies. Two such polars, corresponding to $\tau = 0$ and $\tau = 1$, are illustrated in figure 6(a).

With increasing frequency, both branches of the polars shift to larger values of u until the right-most branch becomes tangent to the shaded region. The intersection of the curve (4.4) with a dispersion-relation polar at some finite angle would indicate that part of the latter would lie in the shaded region where $\Delta < 0$, which is a contradiction. Tangency of the dispersion relation polar to the curve $\Delta = 0$ indicates that a pair of (u, v) are simultaneous solutions of (4.2) and (4.4) and that the scheme is unstable. The corresponding reduced frequency of the forcing is given by

$$\tau(v; F_h, \alpha) = F_h^2 \left[\frac{\Sigma_1(u, v; \alpha)}{\Sigma_0(u, v; \alpha)} \right]_{\Delta=0} \quad (4.5)$$

and is obtained by making use of (4.3). In figure 6(a) this tangency occurs first at the point A for $\tau = \tau_A = 1.48$. For values of $\tau > \tau_A$ the contact point moves from A to B , with corresponding values of τ ranging in $1.48 = \tau_A < \tau < \tau_B = 1.68$. Therefore, the values τ_A and τ_B provide lower and upper bounds, respectively, for the reduced frequencies at which the grid of (F_h, α) results in an unstable numerical scheme.

Figure 6(b) plots the dispersion relation polars for the same grid ($F_h = 1, \alpha = 1$) and

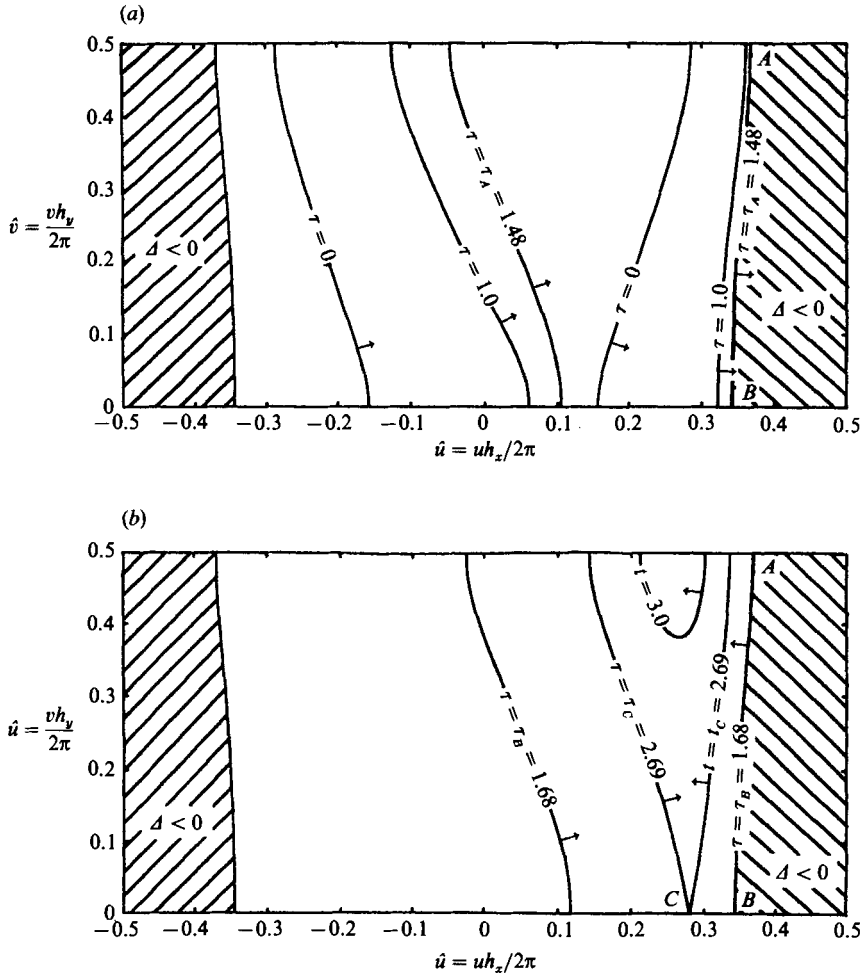


FIGURE 6. The polars of the discrete dispersion relation corresponding to (a) $\tau = 0$, $\tau = 1.0$, $\tau = \tau_A = 1.48$, and (b) $\tau = \tau_B = 1.68$, $\tau = \tau_C = 2.69$, $\tau = 3.0$, for the grid ($F_h = 1$, $\alpha = 1$), over the principal wavenumber domain. The shaded region corresponds to $\Delta < 0$ (equation (4.1)). The right-hand branch of $\tau = \tau_A$ and $\tau = \tau_B$ are tangent to the shaded region at the points A and B respectively. The right- and left-hand branches meet at the point C for $\tau = \tau_C$, while for $\tau = 3.0 > \tau_C$ they merge into a common branch.

three frequencies $\tau = \tau_B = 1.68$, $\tau = \tau_C = 2.69$ and $\tau = 3$. For $\tau = \tau_C$ the two branches of the polar meet on the u -axis and merge into one branch for larger values of τ . Figure 6(b) also plots the vectors normal to these polars which show that the group-velocity vector reverses direction at the point where the polar is tangent to the $\Delta = 0$ curve. This reversal of the group velocity for the wave system corresponding to the right-most branch of the polar relative to the continuous problem is physically unacceptable. Therefore, the numerical solution for any value of τ greater than τ_A is defined to be unstable even when the polar is not tangent to the shaded region.

As discussed in §3, the dispersion-relation polars may exhibit a significantly different topology for other choices of the grid parameters (F_h, α), see e.g. figure 4(b). In this case the shape of the shaded region $\Delta < 0$ changes as shown in figure 7(a, b). The discussion of the preceding paragraphs applies to this topology also. Here, the lower bound of the reduced frequency at which instability occurs is $\tau_A = 0$, owing to

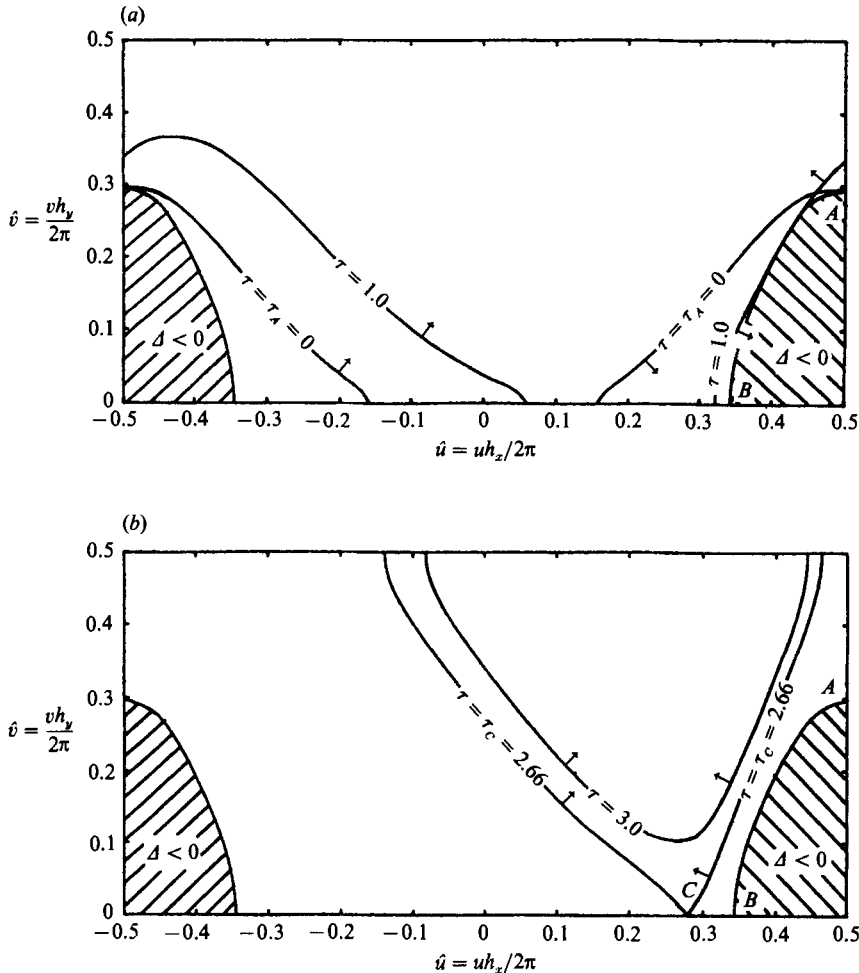


FIGURE 7. The polars of the discrete dispersion relation corresponding to (a) $\tau = \tau_A = 0$, $\tau = 1.0$, and (b) $\tau = \tau_c = 2.66$, $\tau = 3.0$, for the grid ($F_h = 1$, $\alpha = 4$), over the principal wavenumber domain. For this topology the polars for all $\tau \in [0, \tau_B]$ are tangent to the shaded region, where $\Delta < 0$ (equation (4.1)). Note the reversing of the direction of wave propagation along the right-most branch of the polar $\tau = 1$, taking place at the point where the branch becomes tangent to the shaded region ($\Delta < 0$). The right- and left-hand branches meet at the point C for $\tau = \tau_c$, while for $\tau = 3.0 > \tau_c$ they merge into a common branch.

the identity $\Sigma_1(u = \pi/h_x, v; \alpha) = 0$. This indicates that a pole is pinched on real values of (u, v) for all reduced frequencies τ smaller than τ_B , including the steady problem ($\omega = 0, U > 0$). The behaviour of the branches of the polars with increasing frequency is similar to that shown in figure 6(a, b) and is shown in figures 7(a) and 7(b).

It follows that, for any given grid defined by the parameters (F_h, α) , there exists a critical reduced frequency τ_A , such that the discretization leads to a stable and physically acceptable numerical solutions for forcing frequencies $\tau < \tau_A$.

Figure 8 summarizes the results of the stability analysis by plotting in the plane (F_h, α) stability curves corresponding to different values of the reduced frequency τ that subdivide the plane into domains of stability and instability. For example, for the forcing frequency $\tau = 2$ values of (F_h, α) that correspond to a point that lies to the

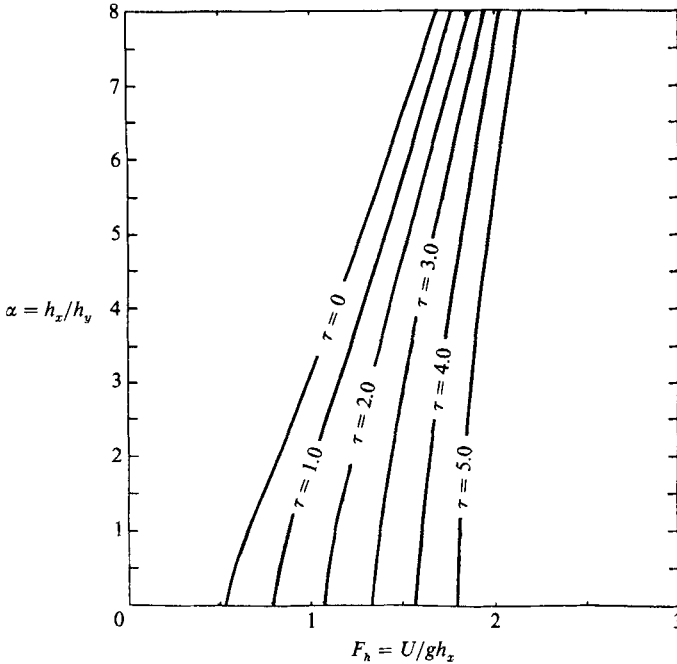


FIGURE 8. The stability diagram for the quadratic-spline scheme. Grids that are mapped on the (F_h, α) -plane at points to the right of a particular curve are stable when used to discretize the problem forced at the reduced frequency τ that corresponds to that particular curve.

right of the corresponding stability curve lead to a stable numerical algorithm. This definition extends to other values of the reduced frequency τ .

The relative positions of the stability curves in figure 8 suggests that a grid (F_h, α) which is stable for a given value of τ will also be stable for all smaller values of the reduced frequency. Therefore, a grid that is stable for the highest reduced frequency of interest in a practical application can and should be used for all smaller frequencies because of the computational savings associated with regriding and the set-up of the solution matrix.

5. Discrete dispersion relations for transient flows

The time-harmonic problem studied in this paper is a special case of flows subject to the more general transient free-surface condition (2.1). The present section outlines extensions of the analysis of §§3 and 4 to flows where the discretization of the free surface is coupled with finite-difference schemes for the approximation of the time derivatives in the free-surface condition. The detailed study of this method will be the subject of future research aiming at the solution of linear, second-order and nonlinear free-surface flows in the time domain.

Consider the free-surface condition (2.1) and apply Green's theorem as in §3 to obtain the integro-differential equation for the velocity potential $\phi(\mathbf{x}, t)$ over the mean position of the free surface

$$\phi(\mathbf{x}, t) + \frac{1}{g} \iint_{FS} \left(\frac{\partial^2}{\partial t^2} + 2U \frac{\partial^2}{\partial t \partial \xi} + U^2 \frac{\partial^2}{\partial \xi^2} \right) \phi(\xi, t) G(\mathbf{x}; \xi) d\xi = \mathcal{R}(\mathbf{x}) e^{i\omega t} H(t), \quad (5.1)$$

where $H(t) = 0, t < 0$ and $H(t) = 1, t > 0$ and ω is a fixed frequency. We study here cosine- or sine-like excitations which start from rest, corresponding to the real and imaginary parts of (5.1) respectively. A more general transient forcing may be studied in a similar manner. Adopting the discretization (3.2) for $\phi(x, t)$ with the weights $a_j(t)$ now being functions of time, and after discrete Fourier transformation in space and continuous Fourier transformation in time, we may represent the numerical solution at the collocation points (x_j, y_j) in the form

$$\phi_n(x_j, y_j, t) = \frac{-i}{(2\pi)^3} \int_{-\infty-i\delta}^{+\infty-i\delta} d\sigma \frac{e^{i\sigma t}}{\sigma - \omega} \iint_{-\infty}^{\infty} du dv \frac{\tilde{f}(u, v)}{\hat{W}(u, v; \sigma; F_h, \alpha)} e^{-iux_j - ivy_j}, \quad (5.2)$$

where \hat{W} is given by (3.6)–(3.13). The frequency contour of integration lies below all singularities of the integrand in the complex σ -plane in order to enforce the causality condition that the solution vanishes for $t < 0$.

The steady-state component of the wave disturbance (5.2) is obtained from the residue of the integrand at $\sigma = \omega$, and may be seen to be identical to expression (3.12), the properties of which have been studied in §§3 and 4. The transient component is associated with the remaining singularities of the integrand in the σ -plane and may be bounded or unbounded in time. The latter case signifies the presence of an instability which may be characterized as absolute or convective by the theory reviewed by Bers (1983).

If the solution of (5.1) is desired at finite time, the time derivatives must be approximated by finite-difference schemes. The resulting solution is discrete in both space and time and may be again cast in the form (5.2), where now the discrete dispersion relation is given by (3.13) and (3.14) with

$$\hat{L}(u, v; \sigma; F_h; \alpha) = \left(\frac{h_x}{g}\right) \Sigma_0(u, v; \alpha) D(\sigma, \Delta t) - 2iF_h \left(\frac{h_x}{g}\right)^{\frac{1}{2}} \Sigma_1(u, v; \alpha) S(\sigma, \Delta t) - F_h^2 \Sigma_2(u, v; \alpha) + 1. \quad (5.3)$$

The operators $D(\sigma, \Delta t)$ and $S(\sigma, \Delta t)$ are the time discrete Fourier transforms of the finite-difference approximations of the double and single time derivatives. In the limit as the time step $\Delta t \rightarrow 0$ they tend to $-\sigma^2$ and $i\sigma$ respectively.

The success of the numerical method analysed in the present paper for linearized time-harmonic and transient flows also depends on the proper enforcement of the radiation condition that the energy of the wave disturbance is absorbed at infinity. The analysis of §§3–5 assumes that the free-surface discretization extends to infinity. In practice the extent of the free-surface grid will be finite and the availability of localized or distributed energy-absorbing conditions is essential. For the forward-speed time-harmonic flow, effective localized conditions are presented in §6. In transient zero- or forward-speed flows absorbing conditions may be obtained by utilizing the theory of this section. Time-marching schemes can be designed that introduce a controllable amount of damping to the numerical wave disturbance, therefore reducing its amplitude. The introduction of numerical damping is desirable only in the vicinity of the boundary of the free-surface discretization, and in practice may be introduced by utilizing time-marching schemes with different properties in different parts of the computational domain.

6. Numerical results

The present section presents computations of steady and unsteady wave patterns generated by a submerged point source, a thin strut and a thick hull form. Solutions for the submerged source and the thin strut can be obtained in the form of inverse Fourier integrals. These solutions will hereafter be referred to as *continuous solutions*, since they do not involve discretization of the geometry nor of the unknown velocity potential. Comparison between the continuous and discrete solutions associated with the aforementioned wave flows is presented in this section and it confirms the convergence properties of the proposed numerical scheme.

Denote by FS the free surface discretized with panels and S_B the wetted surface of the ship. Applying Green's theorem as in §3, the right-hand side of (3.1) becomes

$$\mathcal{R}(\mathbf{x}) = \iint_{S_B} \left(\phi(\xi) \frac{\partial G(\xi; \mathbf{x})}{\partial n_\xi} - G(\xi; \mathbf{x}) \frac{\partial \phi(\xi)}{\partial n_\xi} \right) d\xi, \quad (6.1)$$

where \mathbf{n} is a unit vector normal to S_B pointing out of the fluid domain. If the ship surface is replaced by a point wave source located at $\mathbf{x}_0 = (0, 0, -d)$, the surface S_B may be defined to be a sphere of small radius ϵ centred at \mathbf{x}_0 . The velocity potential $\phi(\xi)$ on its surface behaves locally like $1/\epsilon$ and in the limit as $\epsilon \rightarrow 0$ the expression (6.1) reduces to

$$\mathcal{R}(\mathbf{x}) = \frac{1}{|\mathbf{x} - \mathbf{x}_0|}, \quad (6.2)$$

where \mathbf{x} lies on the free surface. The discretization of (3.1) and (6.1)–(6.2) involves the truncation of the free surface FS upstream, downstream and at some transverse distance from the disturbance and also the distribution of plane quadrilateral panels on FS and on the ship surface S_B . On both surfaces, the velocity potential $\phi(\xi)$ is approximated by the quadratic-spline representation (3.2) defined relative to local panel-fitted coordinate systems. The spatial convective derivatives in the free-surface condition are evaluated by direct differentiation of the underlying basis functions and the integral equation is collocated at the panel centroids. Further details on the discretization are presented in A.

A necessary complement to the stability analysis presented in §§3 and 4 is the enforcement of proper 'radiation' conditions at the boundary of the free-surface grid. In steady forward-speed flows the wave disturbance trails the disturbance and is confined within the Kelvin angle of 19.5° . In time-harmonic flows, no wave systems are present upstream for $\tau = \omega U/g > \frac{1}{4}$, the wave disturbance being confined in a trailing sector with enclosed angle that decreases with increasing τ (Wehausen & Laitone 1960). For the time-harmonic problem results are presented here for $\tau > \frac{1}{4}$, which corresponds to the range of speeds and frequencies of most practical interest in the ship motion problem.

In the steady problem, it is known in A that the condition of no waves upstream may be enforced by truncating the free-surface discretization at a sufficient distance upstream of the disturbance and enforcing the vanishing of both the wave elevation and its slope at the upstream truncation boundary. The corresponding condition in the time-harmonic problem for $\tau > \frac{1}{4}$ is

$$\left(i\omega + U \frac{\partial}{\partial x} \right) \phi = \left(i\omega + U \frac{\partial}{\partial x} \right)^2 \phi = 0. \quad (6.3)$$

The transverse truncation of the free-surface grid is located outside the trailing wave sector and the condition ($\partial^2\phi/\partial y^2 = 0$) is enforced. No condition is enforced at the downstream truncation which intersects the wave pattern. The flow symmetry condition ($\partial\phi/\partial y = 0$) is imposed along the x -axis upstream and downstream of the ship, and the ship-hull normal velocity condition is imposed along its waterline. Finally, the natural spline condition is employed on the hull surface, except on the waterline where continuity of the value of the potential on the free surface and on the hull is enforced. The performance of the algorithm with the interior numerical properties described in §§3 and 4 and the boundary conditions presented in this section is illustrated below.

Figure 9(a) respectively show the continuous and discrete solutions for the steady wave elevation due to a translating point source submerged at $dg/U^2 = 0.3$ below the free surface. The continuous solution (figure 9a) is correct to single-precision accuracy and has been obtained from the evaluation of the Havelock wave source potential using the algorithms developed by Newman (1987) and Clarisse (1989). The free-surface grid used for the computation of the discrete solution is ($F_h = \sqrt{2}, \alpha = 2$) and its extent is shown in figure 9(b). Figure 9(c) shows contour plots of the same wave patterns confirming the very good agreement between the continuous and discrete solutions.

Computations of the steady ship-like pattern generated by a thin strut of uniform vertical geometry, infinite draught and a parabolic waterline are shown in figure 10(a, b, c). For a small strut thickness, the hull boundary condition can be applied on the $y = 0$ plane and Michell's thin-ship theory may be applied to obtain a continuous solution for the wave pattern in terms of Havelock wave sources of known strength distributed on the strut centreplane. The corresponding Kelvin wave pattern downstream of the strut advancing at a Froude number $F = U/(gL)^{1/2} = 0.4$ is shown in figure 10(a) and has been evaluated by Clarisse (1989). The discrete solution for the wave pattern is shown in figure 10(b) and was obtained using the grid ($F_h = \sqrt{2}, \alpha = 2$). The agreement is very satisfactory both for the transverse and the shorter diverging waves which in the numerical solution are seen to persist at a significant distance downstream of the strut owing to the absence of numerical dissipation. The numerical dispersion is also seen to be negligible for the selected values of F_h and α . The accurate prediction of the amplitude and location of both the long and short wave scales in the Kelvin wake is also evident in the contour plot shown in figure 10(c).

Figure 11(a, b, c) illustrates computations of the steady wave pattern generated by the Wigley hull advancing at a Froude number 0.32. The Neumann-Kelvin free-surface condition is used, and the grid, which is shown in figure 11(a), is characterized by $F_h = \sqrt{2}$ and $\alpha = 2$. The hull beam-to-length ratio is 0.1, the draught-to-length ratio is 0.0625 and the waterline and station variation are both parabolic. The contour plots, figure 11(c), illustrates quite clearly the transverse waves and two sets of diverging waves originating from the bow and stern. The extent of the computational domain is that shown in the figure and no wave reflections are seen to occur from its boundaries. For the selected values of F_h and α , 2080 panels are distributed on half the free surface and half the hull, after taking into account the flow symmetry about the $y = 0$ plane.

The real part of the velocity potential of the time-harmonic disturbance flow on the free surface, due to a point source submerged at a distance $dg/U^2 = 0.45$ below the free surface and pulsating at $\tau = 1$ is shown in figure 12(a, b). Figure 12(a) illustrates the discrete solution obtained using the grid ($F_h = 2, \alpha = 2$). In figure 12(b)

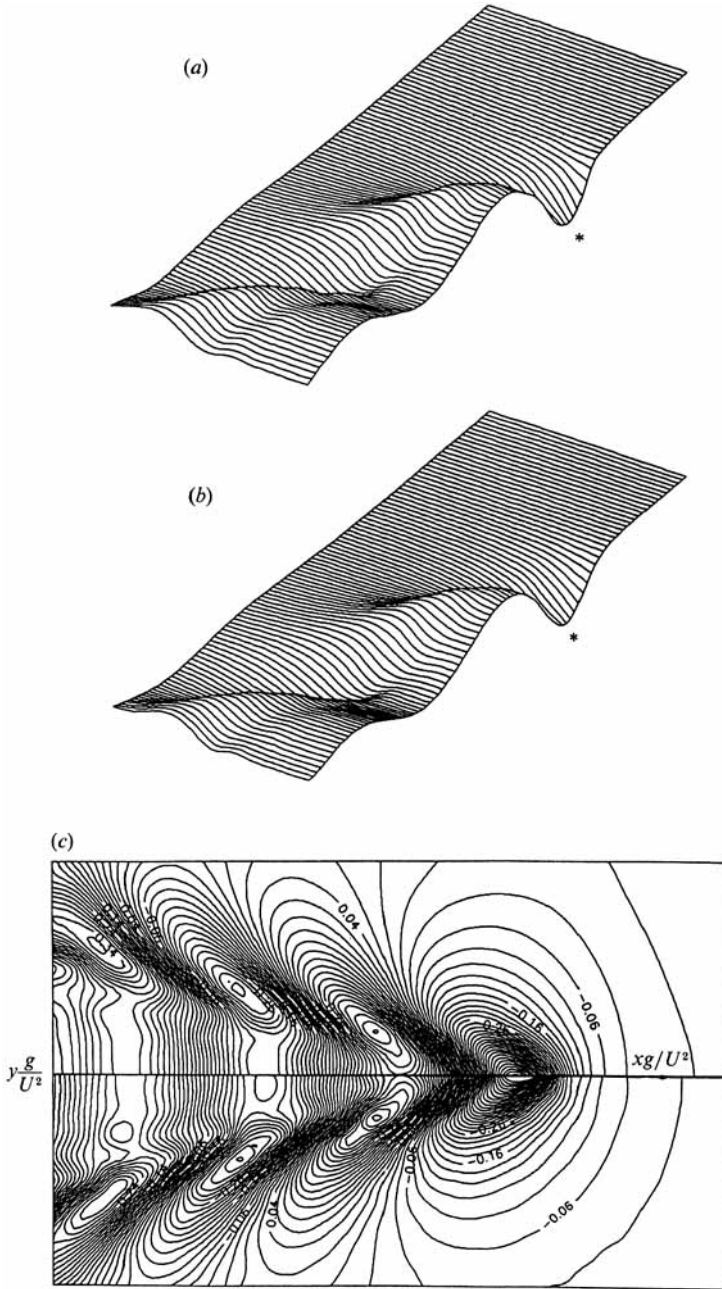


FIGURE 9. (a) The continuous and (b) the discrete solution for the wave field due to a steady Kelvin source submerged at a depth $d = 0.3U^2/g$, where U is the speed of forward translation. The source point is shown in the figures by the asterisk. The grid used for the computation of the discrete solution is ($F_h = \sqrt{2}$, $\alpha = 2$). (c) Contour plots of the wave elevation due to the submerged Kelvin source of (a): comparison between the discrete solution (top half) and the continuous solution (bottom half).

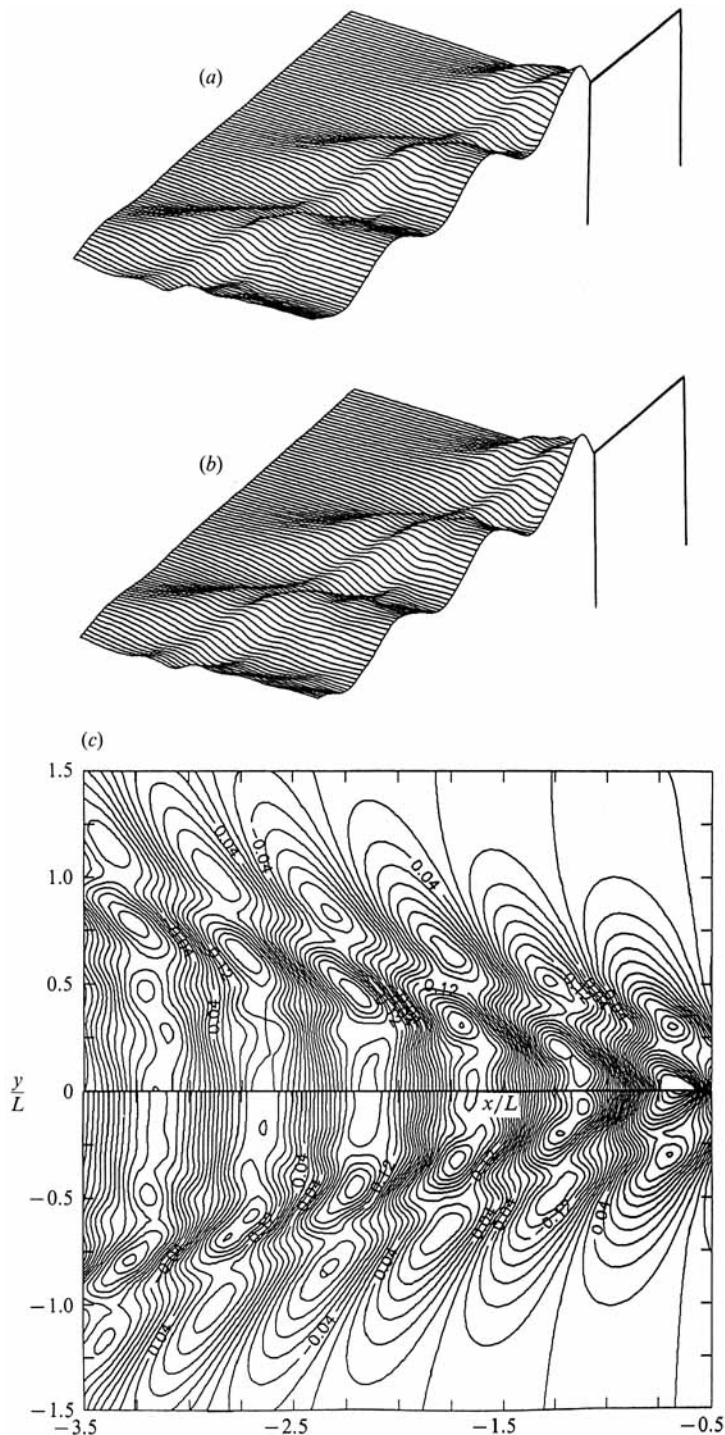


FIGURE 10. (a) The continuous and (b) the discrete solution for the wave elevation due to a 'thin strut' advancing at Froude Number $F = 0.4$. The 'thin strut' has parabolic waterlines with beam-to-length ratio $B/L = 0.1$, uniform geometry in the vertical direction and infinite draught. The grid used for the computation of the discrete solution is ($F_h = \sqrt{2}$, $\alpha = 2$) and consists of 1200 panels on half the free surface. (c) Contour plots of the wave elevation due to the 'thin strut' of (a): comparison between the discrete solution (top half) and the continuous solution (bottom half).

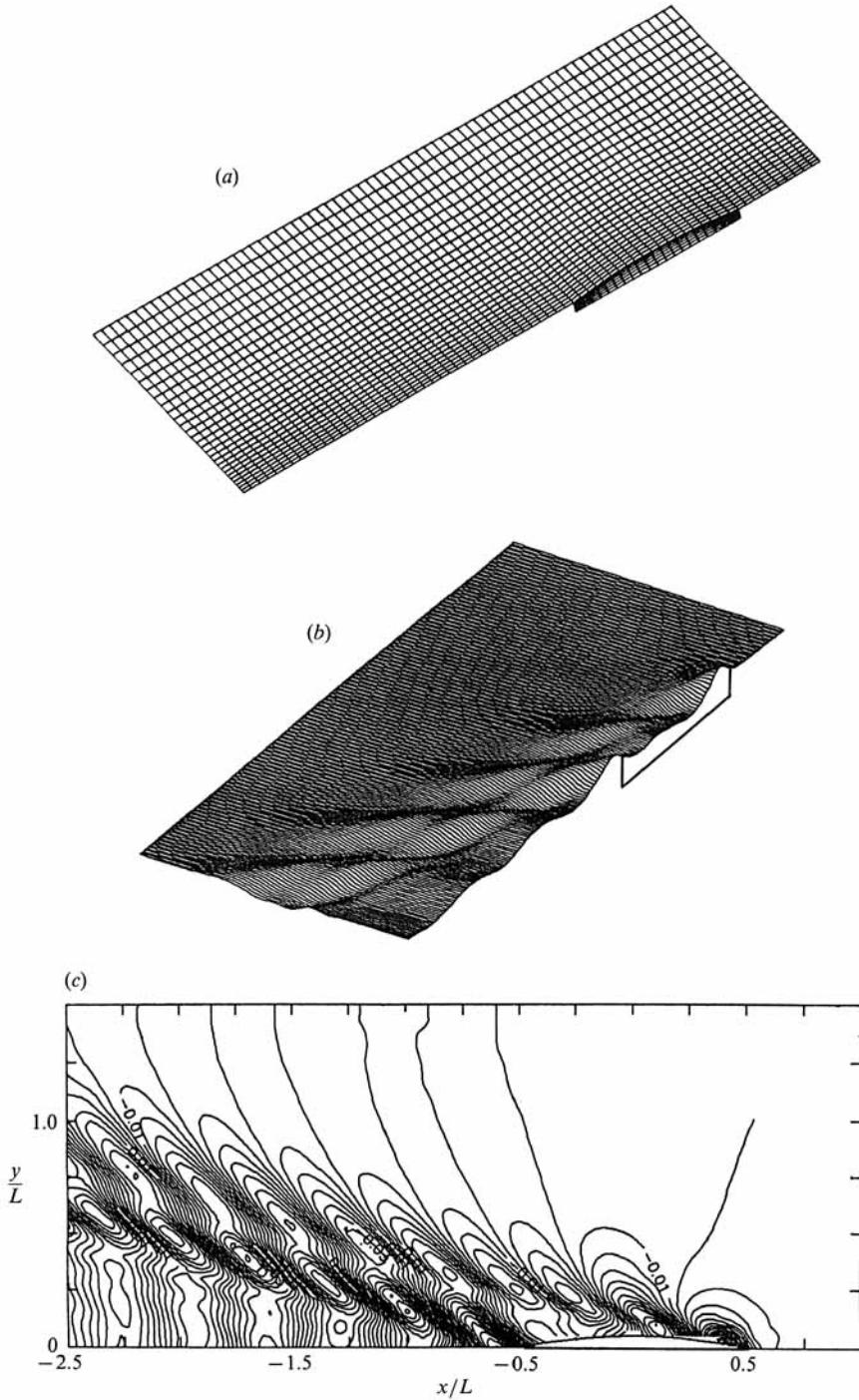


FIGURE 11. (a) The grid used for the solution of the steady wave flow around the Wigley hull advancing at Froude number $F = 0.32$. The grid parameters are ($F_h = \sqrt{2}$, $\alpha = 2$) and it consists of 1960 panels on half the free surface and 120 panels on half the hull surface. The Wigley hull is defined by both parabolic waterlines and sections, with beam-to-length ratio $B/L = 0.1$ and draught-to-length ratio $D/L = 0.0625$. (b) Prospective view and (c) contour plots of the discrete solution for the wave elevation around the Wigley hull advancing at Froude Number $F = 0.32$, using the grid shown in (a).

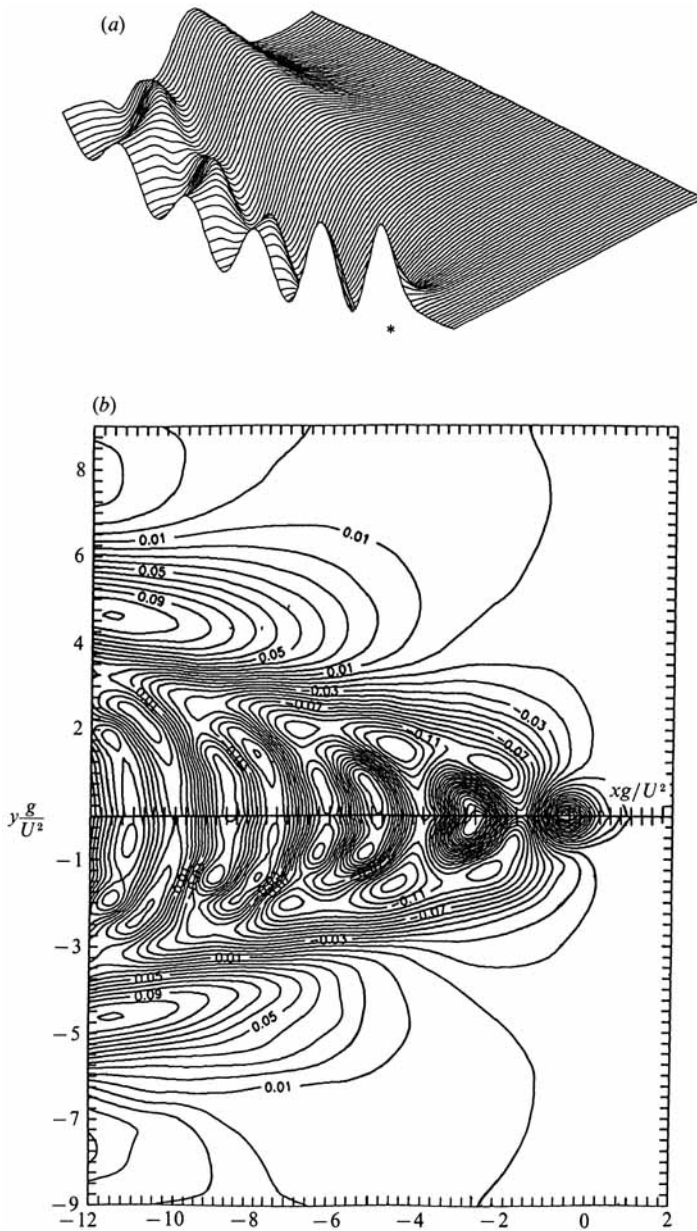


FIGURE 12. (a) The real part of the discrete solution for the velocity potential on the free surface due to a submerged point source with a time-harmonically oscillating strength. The source is shown by the asterisk and is submerged at a depth $d = 0.45U^2/g$, where U is the speed of forward motion, and the reduced frequency of oscillation is $\tau = 1.0$. The grid used for these computations is $(F_h = 2, \alpha = 2)$. (b) Contour plots of the real part of the velocity potential on the free surface due to the time-harmonic wave source of (a): comparison between the discrete solution (top half) and the continuous solution (bottom half).

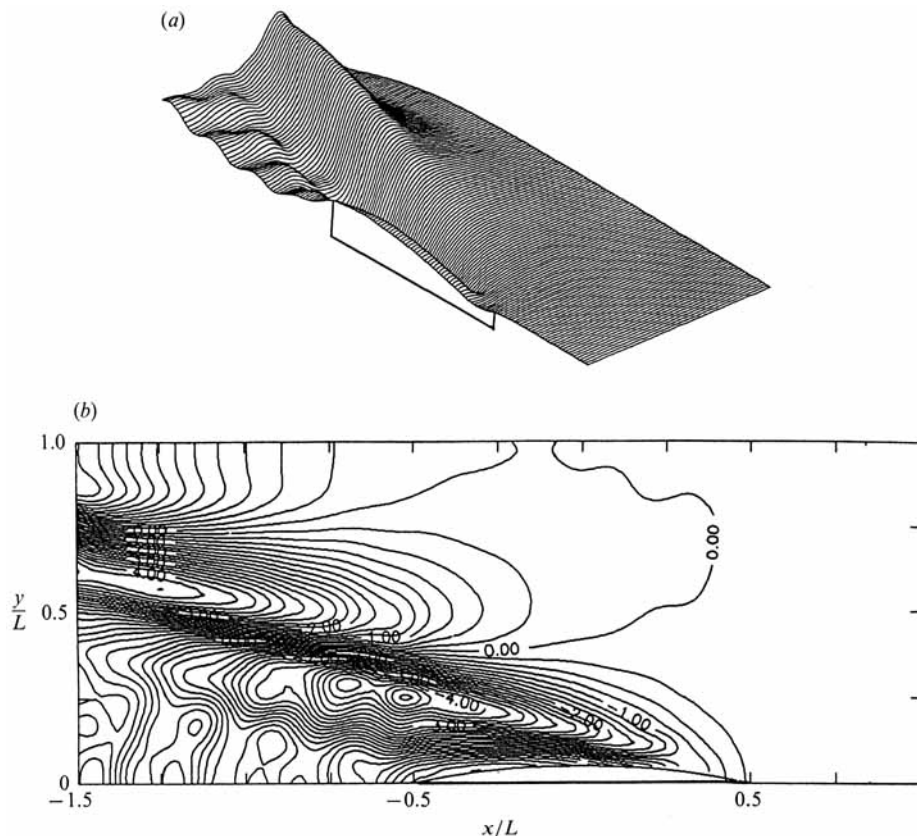


FIGURE 13. The real part of the discrete solution for the wave elevation around the Wigley hull (figure 11*a*) advancing at Froude Number $F = 0.32$ while undergoing a time-harmonic heave oscillation at reduced frequency $\tau = 1.0$. The grid used for these computations is ($F_h = 2, \alpha = 2$) and consists of 2068 panels on half the free surface and 240 on half the ship surface. (a) Prospective view and (b) contour plots.

the discrete solution is compared with the continuous solution, obtained from the explicit expression for the time-harmonic wave source potential (see e.g. Wahausen & Laitone 1960). Two wave systems, consisting of quite disparate lengthscales, are present in figure 12 and are both accurately described by the numerical solution. Each corresponds to a branch of the dispersion relation polar plotted in figure 4. The right branch of the $\tau = 1$ polar in the (u, v) -plane corresponds to the wave system consisting of short transverse and diverging waves which are clearly visible in figure 12(*a*). The transverse waves of the wave system corresponding to the left branch of the same polar are less evident but may be seen to modulate the short waves along the track of the source. The crests of the diverging waves of the same system are nearly parallel to the x -axis, which may be verified from figure 4(*a*) by observing that the u -wavenumber of the inflection point of the corresponding branch is nearly zero.

Finally figures 13(*a*) and 13(*b*) show the discrete solution for the real part of the time-harmonic wave elevation around the Wigley hull advancing at a Froude number 0.32 and forced in a time-harmonic heave oscillation at $\tau = 1$. Notable is the absence of the transverse or divergent components of the wave system along the ship hull, attributed to cancellation effects.

7. Summary

The stability properties and performance of a Rankine panel method are studied for the prediction of steady and time-harmonic ship wave patterns. It is shown that the propagation of the wave disturbance over the discretized free surface is governed by a discrete dispersion relation. Comparison with its continuous counterpart permits the rational analysis of the numerical properties of the selected computational scheme which is shown to be free of numerical damping and possess a numerical dispersion of cubic order. The discrete dispersion relation is also used to derive a numerical stability criterion which restricts the selection of the grid Froude number relative to the aspect ratio of the panels used to discretize the free surface.

Computations were carried out of the steady and time-harmonic wave patterns around elementary singularities, a thin strut and a realistic ship form. Comparison with analytical solutions confirms the numerical qualities and convergence of the algorithm which, owing to the absence of numerical damping, is capable of resolving and propagating a significant distance downstream short scales in the wave pattern. The accurate computation of the steady and unsteady wave patterns permits the implementation of this numerical algorithm for the evaluation of the wave resistance acting on a ship in calm water as well as the time-harmonic hydrodynamic forces and motions of ships in regular waves.

The methodology is outlined for the extension of the present algorithm to three-dimensional transient free-surface flows. The associated numerical analysis can also be extended to schemes for fully nonlinear free-surface flows and will permit the understanding and fundamental resolution of the numerical instability present in quasi-Lagrangian algorithms for the solution of fully nonlinear zero- and forward-speed free-surface flows.

This study has been supported by the Applied Hydromechanics Research Program (contract number N00167-86-K-0010), administered by the Office of Naval Research and the David Taylor Research Center. The computations have been performed on the CRAY YMP of the Pittsburgh Supercomputing Center (Grant number OCE8980003P).

REFERENCES

- AANESLAND, V. 1986 A theoretical and numerical study of the ship wave resistance. Ph.D. dissertation, Department of Marine Technology, The Norwegian Institute of Technology, Trondheim, Norway.
- BERS, A. 1983 Space-time evolution of plasma instabilities – absolute and convective. *Handbook of Plasma Physics*, vol. 1, Chapter 3.2.
- CLARISSE, J. M. 1989 On the numerical evaluation of the Neumann–Kelvin Green Function. SM thesis, Department of Ocean Engineering, MIT, USA.
- DAWSON, D. W. 1977 A practical computer method for solving ship-wave problems. *2nd Intl Conf. on Numerical Ship Hydrodynamics*.
- JENSEN, G. 1988 Numerical solution of the nonlinear ship wave resistance problem. *3rd Intl Workshop on water waves and floating bodies*.
- JENSEN, G., MI, Z. X. & SÖDING, H. 1986 Rankine source methods for numerical solutions of the steady ship wave resistance problem. *16th Symp. on Naval Hydrodynamics*.
- JENSEN, P. S. 1987 On the numerical radiation condition in the steady-state ship wave problem. *J. Ship Res.* **31**, pp. 14–22.
- LIGHTHILL, M. J. 1960 Studies on magneto-hydrodynamic waves and other anisotropic wave motions. *Phil. Trans. R. Soc. Lond.* A **252**, 397–430.

- NEWMAN, J. N. 1987 Evaluation of the wave-resistance Green function: Part 1 – The double integral. *J. Ship Res.* **31**, 79–90.
- NI, S. Y. 1987 Higher order panel methods for potential flows with linear or nonlinear free surface boundary conditions. Ph.D. dissertation, Division of Marine Hydrodynamics, Chalmers University of Technology, Göteborg, Sweden.
- RAVEN, H. C. 1988 Variations on a theme by Dawson. *17th Symp. on Naval Hydrodynamics*.
- SCLAVOUNOS, P. D. & NAKOS, D. E. 1988 Stability analysis of panel methods for free surface flows with forward speed. *17th Symp. on Naval Hydrodynamics* (referred to as A).
- VAN BEEK, C. M., PIERS, W. J. & SLOOF, J. W. 1985 Boundary integral methods for computation of the potential flow about ship configurations with lift and free surface effects. *NLR Rep.* TR-85-142 U.
- WEHAUSEN, J. V. & LAITONE, E. V. 1960 Surface waves. In *Handbuch der Physik*, vol. 9, pp. 446–778. Springer.
- XIA, F. & LARSSON, L. 1986 A calculation method for the lifting potential flow around yawed surface piercing 3-D bodies. *16th Symp. on Naval Hydrodynamics*.